

# From Classical Superposition of Waves to Quantum Interference: Three Level Quantum System for Two Entangled Photons

AMIR DJALALIAN-ASSL<sup>1,\*</sup>

[\\*amir.djalalian@gmail.com](mailto:*amir.djalalian@gmail.com)

**Abstract:** Properties and applications of a plasmonic cross-shaped nano-antenna is presented and compared to those of a bi-periodic array of holes. A simple analytical model based on the superposition of waves are proposed and compared to the numerical results. A direct consequence of unequal path for two orthogonal surface waves leads to a coherent quantum interferometer with interesting properties. Mechanism behind the rotating surface charge densities and consequently, the formation of rotating resultant dipole moments is identified and the concept of Dipole-SPP-LSP-Stokes coupling is introduced. Among the most significant findings, a three-level quantum system for entangled photons, based on the polarization state of the transmitted light is presented.

## 1. Introduction

A single photon source emits energy in the form of one quantized unit of light at a time. Controlling the polarization state of a Single Photon Source (SPS) provides a mechanism for defining the computational basis states [1-3]. A more elaborated account on the photon statistics related to the bunched, coherence, anti-bunched, single photon states, entangled photons and second order correlation function  $g^2(0)$  can be found in [4, 5]. The driving force behind the development of SPSs and single photon detectors is mainly the quantum information science, including cryptography [6]. Quantum cryptography based on Bell's theorem was first outlined in [7], where the polarized photons were proposed as a replacement for the  $\frac{1}{2}$ -spin particle interactions. The quantum mechanics and the algorithms behind the cryptography are elaborated on in [8] and beyond the scope of this report. Suffice to say that the two requirements, i.e. individual quanta and the entangled states could be satisfied by the polarization states of photons. Furthermore, it was argued that the vertical or the horizontal polarization states can only be defined relative to the emitter's and/or detector's position and orientation, hence not suitable for real-life applications. Therefore, to form the computational basis states, the left-handed and the right-handed circular polarization are more suitable [2]. However, to generate circularly polarized light (CPL) at least two photons are needed. For a brief background on circularly polarized light, ellipticity, amplitude and the phase requirements of the two constituting orthogonal modes see chapter 2 of my master thesis [9]. Basically, to produce CPL, there must exist two orthogonal optical sources that satisfy two conditions: **(A)** The phase difference between the two must be  $\pm 90^\circ$ , and **(B)** The two modes must be equal in amplitudes. I have previously reported on plasmonic devices as a possible approach to achieve this [10-12]. Due to the time constrains and page limitations, however, I refrained from reporting on interim effects relating the state of polarization observed in the transmitted light through a plasmonic device and the surface activities. In this report I intend to cover all relevant fundamental effects I have observed to date. This report is divided into two headings organized in a chronological order, describing gradual development of ideas and notions. Some findings were based on initial hypothesis subject to careful design, but some were based on serendipitous observations of results during the tasks related to the former, which I would highlight under subheadings, *Significant Observations*.

## 2. Asymmetric Cross-shaped Nano-antenna

An *Oscillating* electric dipole moment is defined by  $\boldsymbol{\mu}_e(t) = \boldsymbol{\mu}e^{-i\omega t} = Q\mathbf{d}e^{-i\omega t}$  [13], where  $Q$  is the charge and  $\mathbf{d}$  is the vector distance from  $-Q$  to  $+Q$ , that defines the dipole axis by a unit vector  $\hat{\mathbf{d}} = \boldsymbol{\mu}_e / \|\boldsymbol{\mu}_e\| = \mathbf{d} / \|\mathbf{d}\|$ , where double bars signify the magnitude of the vectors. Here,  $\omega = c/\lambda_0$  is the frequency and  $\lambda_0$  the vacuum wavelength. Oscillations of charge densities along the two armlengths of a cross-shaped nano-antenna are of Localized Surface Plasmons (LSP) by nature and may be considered as the resultant (or vector sum) of the two orthogonal dipole moments,  $\boldsymbol{\mu}_x = L_x Q_x \hat{\mathbf{x}}$ ,  $\boldsymbol{\mu}_y = L_y Q_y \hat{\mathbf{y}}$ . Quantities  $L_{x,y} Q_{x,y}$  are the magnitude of electric dipole associated with induced charges  $Q_{x,y}$  at the tips of the armlengths with  $L_{x,y}$ . Considering a linearly polarized light  $\mathbf{E}_i = (E_x \hat{\mathbf{x}} + E_y \hat{\mathbf{y}})e^{-i\omega t}$  with a polarizations angle  $\alpha = \tan^{-1}[E_y/E_x]$  impinging on the cross at normal incidence, induced charges are  $Q_x \propto E_0 A_x \cos(\alpha)$  and  $Q_y \propto E_0 A_y \sin(\alpha)$ , where  $E_0 = \sqrt{E_x^2 + E_y^2}$ . Here,  $A_{x,y}$  are factors encapsulating all other intrinsic physical effects, that contribute to the suppression/excitation of the modes. Consequently  $\boldsymbol{\mu}_x = E_0 L_x A_x \cos(\alpha) \hat{\mathbf{x}}$  and  $\boldsymbol{\mu}_y = E_0 L_y A_y \sin(\alpha) \hat{\mathbf{y}}$ . In other words, the cross and all its intrinsic physical properties operate on the incident field to produce its own dipole moments:

$$\begin{bmatrix} L_x A_x & 0 & 0 \\ 0 & L_y A_y & 0 \\ 0 & 0 & 1 \end{bmatrix} \begin{bmatrix} E_0 \cos(\alpha) \\ E_0 \sin(\alpha) \\ 0 \end{bmatrix} = \frac{1}{\sqrt{2}} \begin{bmatrix} \boldsymbol{\mu}_x e^{-i\omega t} \\ \boldsymbol{\mu}_y e^{-i(\omega t \pm \Phi)} \\ 0 \end{bmatrix} \quad (1)$$

I have already shown that a cross-shaped aperture in a silver film possesses a well-defined virtual dipole moment [14]. Therefore, the analysis on dipolar activities of a cross-shaped nano-particle is also valid with respect to cross-shaped apertures, with  $\boldsymbol{\mu}_x = E_0 L_x A_x \sin(\alpha) \hat{\mathbf{x}}$  and  $\boldsymbol{\mu}_y = E_0 L_y A_y \cos(\alpha) \hat{\mathbf{y}}$ . The resultant dipole moment being the RHS of equation (1) is of interest here and may be written as:

$$\boldsymbol{\mu}_e(t) = (\boldsymbol{\mu}_x e^{-i\omega t} + \boldsymbol{\mu}_y e^{-i(\omega t \pm \Phi)}) / \sqrt{2} \quad (2)$$

That is the superposition of the two orthogonal dipole states. Here, the phase difference,  $\Phi$ , is to cater for  $L_x \neq L_y$ . However, in contrary to the classical dipole where  $\mathbf{d}$  has a physical meaning, the resultant dipole and its axis in this case are purely virtual and dependent on all the factors mentioned above, hence in some cases  $\mathbf{d}/\|\mathbf{d}\|$  is meaningless. Instead the unit vector for the dipole axis must be calculated using  $\hat{\mathbf{d}} = \boldsymbol{\mu}_e / \|\boldsymbol{\mu}_e\|$  which is valid in all cases. As an example, consider a simple case of a *symmetric* cross with  $L_x = L_y$  and  $A_x = A_y$ , where  $\alpha = 45^\circ$  leads to  $\boldsymbol{\mu}_x = \boldsymbol{\mu}_y$  and  $\Phi = 0$ . In this case, the direction of the resultant dipole and the unit vector defining the its axis is given by:

$$\hat{\mathbf{d}}_{lin} = (\boldsymbol{\mu}_x + \boldsymbol{\mu}_y) / \|\boldsymbol{\mu}_x + \boldsymbol{\mu}_y\| = (\hat{\mathbf{x}} + \hat{\mathbf{y}}) / \sqrt{2} \quad (3)$$

and when acted on by the oscillating term  $e^{-i\omega t}$ , it would experience a time harmonic change in direction along the  $\{-135^\circ, 45^\circ\}$  line with respect to the  $x$ -axis. Let us denote equation (3) as a *linear unit vector* hence the subscript “*lin*”. In fact, for a symmetric cross,  $\hat{\mathbf{d}}_{lin}$  aligns itself with  $\alpha$  for all values of  $\alpha$  and  $\lambda_0$ , with the far-field radiation pattern being that of a classical

oscillating dipole, that is toroidal in shape, where the field intensity dropping to zero along  $\hat{\mathbf{d}}_{lin}$ . These were confirmed numerically. For a typical radiation pattern of an oscillating dipole see [13]. Now, consider another simple scenario with respect to an *asymmetric* cross. Let us assume that for some  $\alpha$  and  $\lambda_0$ , conditions (A) and (B) are satisfied, leading to  $\boldsymbol{\mu}_x = \boldsymbol{\mu}_y$  and  $\Phi = 90^\circ$ . In this case:

$$\hat{\mathbf{d}}_{cir} = (\boldsymbol{\mu}_x + \boldsymbol{\mu}_y e^{-i(\pi/2)}) / \|\boldsymbol{\mu}_x + \boldsymbol{\mu}_y e^{-i(\pi/2)}\| = (\hat{\mathbf{x}} - i\hat{\mathbf{y}}) / \sqrt{2} \quad (4)$$

that is complex phasor when operated on by the oscillating term  $e^{-i\omega t}$ , hence  $\hat{\mathbf{d}}_{cir}$  not being confined to any linear direction in the  $x$ - $y$  plane (i.e. the antenna plane), but instead rotating about the  $z$ -axis (i.e. the optical axis) while maintaining its unit magnitude at all time. For a lack of a better term, let us call it a *circular unit vector*.

I presented the asymmetric cross-shaped nano-antenna and the concept of resultant dipole moment in a poster session [15] with relevant figures included here, see also section 4.3 of my thesis[16]. I have described the relevant aspects of the numerical modelling in [17]. The only difference here is the use of asymmetric copper cross rather than the gold nano-rods. Spectra in Figure 1(a) shows the numerical results of an asymmetric cross-shaped nano-antenna, vs the wavelength when excited by a normally incident linearly polarized light polarized in the range  $0^\circ \leq \alpha \leq 90^\circ$ . Radar Cross-Section,  $RCS \propto |E_{far}|^2 / |E_i|^2$ , was calculated in the  $x$ - $y$  plane from the scattered far-field  $E_{far}$  and the background field  $E_i$ . The two orthogonal modes at  $\lambda_{res1} = 820$  nm and  $\lambda_{res2} = 890$  nm are associated with  $L_x = 80$  nm and  $L_y = 95$  nm respectively. To excite the two modes equally,  $\alpha$  was set to  $32^\circ$  from the  $x$ -axis. Naturally, due the separation of the two resonances,  $\Phi \neq 0$ . Figure 1(b) shows the far-field radiation patterns with  $\alpha = 32^\circ$  in the range of  $\lambda_{res1} \leq \lambda_0 \leq \lambda_{res2}$ .

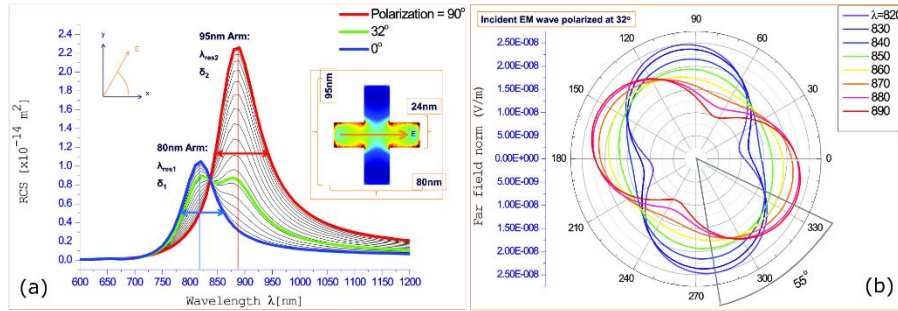


Figure 1: (a) Radar cross-section,  $RCS \propto |E_{far}|^2 / |E_i|^2$ , calculated in the  $x$ - $y$  plane from the scattered far-field  $E_{far}$  and the background field  $E_i$ . (b) Far-field radiation patterns for  $\lambda_{res1} \leq \lambda_0 \leq \lambda_{res2}$  in the  $x$ - $y$  plane with  $\alpha = 32^\circ$ , when the two orthogonal modes are equally excited.

The angular changes in radiations vs the incident wavelength were comparable to those of the gold “T” antenna [17]. But unlike the “T” antenna, far-field radiation patterns of an asymmetric cross showed a  $180^\circ$  rotational symmetry. More importantly, the radiation pattern associated with  $\lambda_0 = c/\omega = 850$  nm was close to a perfect circle. That was an evidence of perpetual rotation of the resultant dipole moment about the  $z$ -axis driven only by the time harmonic term  $e^{-i\omega t}$ . In other words, the dipole axis was defined purely by  $\hat{\mathbf{d}}_{cir}$ . For other values of  $\lambda_0$ , radiation patterns were elliptic, never dropping to zero, suggesting superpositions of two kinds of dipolar

activities, hence  $\hat{\mathbf{d}} = (a\hat{\mathbf{d}}_{lin} + b\hat{\mathbf{d}}_{cir}) / \|a\hat{\mathbf{d}}_{lin} + b\hat{\mathbf{d}}_{cir}\|$ , where  $a, b$  signifies the strength of each type of dipole in the sum.

I reported a similar concept with respect to an asymmetric cross-shaped aperture in a bullseye (BE) setting in a silver screen [10] which revealed the correlation between surface effects and the transmitted state of polarization. The model consisted of a cross-shaped aperture with  $L_x = 150$  nm and  $L_y = 220$  nm at the center of a BE structure with concentric circular corrugations having an inner radius,  $r_{in} = 710$  nm and a period  $P = 650$  nm. Dimensions were optimized for  $\lambda_0 = 700$  nm. Device was illuminated by a normally incident linearly polarized light at  $\lambda_0 = 700$  nm from the glass substrate, and the state of polarization was calculated from the transmitted field. Figure 2(a) shows the numerically calculated Stokes parameters obtained from the transmitted field vs  $\alpha$ . Here  $S_1, S_2$  and  $S_3$  range from -1 to 1, signifying degrees of vertical/horizontal, diagonal and circular polarizations respectively. Figure 2(b) depicts the surface charge densities calculated at  $\alpha = 90^\circ$  where the transmitted field showed  $S_3 = S_2 = 0$  and  $S_1 = -1$ . Figure 2(c) represents the spiral surface charge densities launched by the cross when  $\alpha = 46^\circ$  corresponding to  $S_1 = S_2 = 0$  and  $S_3 = 1$ . Consequently, a clear link between the transmitted state of polarization and the surface effects was possible by inference.

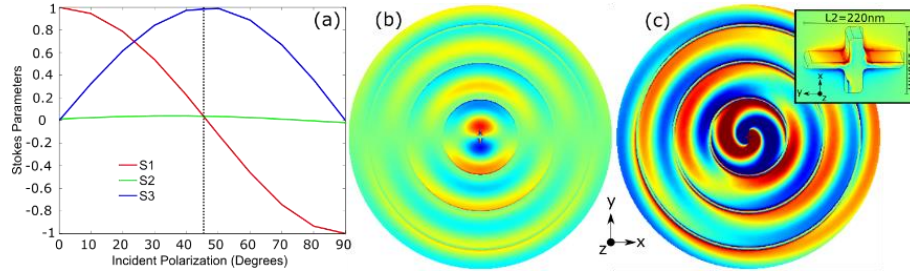


Figure 2: (a) Calculated Stokes parameters obtained from the transmitted field through an isolated cross-shaped aperture with  $L_x = 220$  nm and  $L_y = 150$  nm, vs  $\alpha$ . (b) Surface charge densities calculated at  $\alpha = 90^\circ$  related to the transmitted state of polarization  $S_3 = S_2 = 0$  and  $S_1 = -1$ . (c) Spiral surface charge densities produced when  $\alpha = 46^\circ$ , with the transmitted state of polarization  $S_1 = S_2 = 0$  and  $S_3 = 1$ . Inset shows LSPs inside the aperture.

## 2.1 Significant Observations and Applications

### 2.1.1 Applications in Radiofrequency Antennas

In general, there are strong analogies between optical and radiofrequency (RF) dipole antennas. One can hypothesize on a pair of orthogonal RF dipole antennas satisfying conditions (A) and (B). Consider the normal vector  $\mathbf{n}_r$  defining the plane of the resultant dipole moment such that  $\boldsymbol{\mu}_x \perp \boldsymbol{\mu}_y \perp \mathbf{n}_r$ . From Figure 2(c), one can intuitively infer that the radiation from such a pair adheres to  $\mathbf{E} \perp \mathbf{n}_r$  for all  $\mathbf{k} \perp \mathbf{n}_r$ , eliminating the need for mechanically driven revolving RF dipole antennas. Here  $\mathbf{k}$  is the wavevector defining the direction of propagation from the resultant dipole to the point of observation and  $\mathbf{E}$  is the electric field vector. Naturally, when considering the transmission of such a pair along  $\mathbf{k} \parallel \mathbf{n}_r$ , circularly polarized radio waves (CPRW) would be detected, and that may have applications in astronomy, just as CPL has applications in microscopy.

### 2.1.2 Dipole-SPP-LSP-Stokes coupling

Figure 2(b) and Figure 2(c) are clear signs of dipolar activities associated with  $\hat{\mathbf{d}}_{lin}$  and  $\hat{\mathbf{d}}_{cir}$ . Correlation between the transmitted state of polarization and the surface activities such as SPPs, LSPs and  $\hat{\mathbf{d}}$  was established, meaning that by measuring the transmitted state of polarization one could infer the state of SPP, LSP on the surface and ultimately  $\hat{\mathbf{d}}$  inside the aperture. This

dipole-SPP-LSP-Stokes coupling inferred that rotating surface waves may induce rotating resultant dipole moments inside symmetric apertures such as circular holes. But before getting into that, I would highlight the experimental aspects related to the plasmonic bullseye structure presented above, and the consequential restraints on its optical response, when fabricated dimensions divert from those intended by design.

### 2.1.3 Mechanism governing the spiral surface waves

The magnetic field associated with the resultant dipole moment above, though orthogonal to the electric field, rotates in the  $x$ - $y$  plane and about the  $z$ -axis just as the electric field does. Hypothetically, it is possible for a constant magnetic field,  $B_z$  in the  $z$ -direction, either applied externally or established by the hole, to induce cyclotronic electrons inside or in the vicinity of the hole that rotate about the  $z$ -axis. In a flat metallic slab the cyclotron resonance has a frequency [18]:

$$\omega_c = \frac{eB_z}{m^*} \quad (5)$$

where  $e$  is the charge and  $m^*$  is the effective mass of the electron, hence clearly a function of  $B_z$ . Whereas my numerical results confirmed the rotation frequency of the spiral to be  $\omega_0 = 2\pi/T$  where  $\omega_0$  and  $T$  are the frequency and the period of the incident wave respectively. Furthermore, my numerical analysis and experiments were carried out in the absence of any applied magnetic field. Consequently, at this stage, I tend to eliminate any possible scenarios where any cyclotronic electrons being formed inside or near the aperture when the device is excited with an incident light at  $\lambda_0 = 700$  nm and  $\alpha = 46^\circ$ . Nevertheless, a future study on plasmonic holes with constant magnetic field,  $\pm B_z$  applied externally, while the device is excited with an incident light, would make an interesting research project. How does  $\pm B_z$  impacts the SPPs? How the presence of a metallic hole impact the  $\omega_c$ ? Alternatively, in the absence of any incident light, could such cyclotrons match the SPP's momentum, so to ignite a spiral or any other type of SPPs at some frequency? And if so, could this lead to any scattered EM wave into the free-space. These are among many other questions remains to be answered.

What I believe is governing the spiral nature of the surface waves in this report are as follow. I have reported on the SPP waves launched under the forced vibration by a virtual dipole of an aperture previously [14, 19]. The only difference here is the formation of the resultant dipole moment and its spin angular momentum, when the device is excited with an incident light at  $\lambda_0 = 700$  nm and  $\alpha = 46^\circ$ . The angular frequency of the spiral about the  $z$ -axis is that of the drive,  $\omega_0$ , as I mentioned above. Meaning that the resultant dipole has a time dependent orientation in the  $x$ - $y$  plane,  $\theta_{\text{dipole}}(t) = \omega_0 t$ , while continuously launching SPPs. Nevertheless, SPPs propagate radially away from the aperture with the wavevector,  $\mathbf{k}_{\text{SPP}}$ , in directions that are time lapsed, and as such there is no intrinsic orbital or spin angular moment involved in  $\mathbf{k}_{\text{SPP}}$ . The spiral appearance of the surface charge densities is purely due to the time lapsed between the consecutive points that are in phase yet conceived at different points in time. Any set of such points on surface waves, may be traced along a single strand of an Archimedean spiral line, such as  $\frac{\lambda_{\text{SPP}}}{2\pi} \theta_{\text{SPP}}$ , if expressed in polar coordinates. For a given phase,  $\phi_j$ , where  $j$  is an integer, a single strand on the spiral SPP may be described in Cartesian coordinates:

$$\begin{bmatrix} x(t, \phi_j, \theta_{\text{SPP}}) \\ y(t, \phi_j, \theta_{\text{SPP}}) \end{bmatrix} = \begin{bmatrix} \text{Cos}[\omega_0 t] & \text{Sin}[\omega_0 t] \\ -\text{Sin}[\omega_0 t] & \text{Cos}[\omega_0 t] \end{bmatrix} \begin{bmatrix} \text{Cos}[\phi_j] & \text{Sin}[\phi_j] \\ -\text{Sin}[\phi_j] & \text{Cos}[\phi_j] \end{bmatrix} \begin{bmatrix} \frac{\lambda_{\text{SPP}} \theta_{\text{SPP}} \text{Cos}(\theta_{\text{SPP}})}{2\pi} \\ \frac{\lambda_{\text{SPP}} \theta_{\text{SPP}} \text{Sin}(\theta_{\text{SPP}})}{2\pi} \end{bmatrix} \quad (6)$$

where the first and the second term on the RHD are the rotation/transformation matrices catering for the time dependent rotation and the phase strand, and the third term is the Archimedean spiral vector catering for the special distribution of SPPs. Note that for simplicity, above equations were derived in the absence of any corrugation. To include the impact of the corrugations one must also incorporate the superposition of forward and reflected backward propagating SPPs as I reported in [14]. Nevertheless, the mechanism governing the spiral waves remain essentially the same.

## 2.2 Experimental Demonstration

Based on the target dimensions obtained from the numerical models, my first attempt to fabricate the device was less than satisfactory, compare the target dimensions above to the those in Figure 3(a). In summary,  $L_x = 200$  nm,  $L_y = 270$  nm,  $707 \leq r_{in} \leq 738$  nm and  $P = 630$  nm. Moreover, spectral measurements seen in Figure 3(b), did not reveal the presence of the two sought orthogonal modes, at least not clearly. Thus, the optimum value for  $\alpha$  could not be determined. Despite my previous suggestion and I quote: "The peak at  $\lambda=715$  nm which is present in all cases, is attributed to both the SPP Bloch mode associated to the periodic corrugations and the LSPR associated with the shorter arm of the asymmetric cross.[10]", though a probable cause, one must not dismiss other factors such as the off-center position of the cross with respect to the center of the corrugations, hence yet another two modes associated with the inner circle. Given that  $S_3$  parameter peaked at  $\lambda_0 = 715$  nm, see Figure 3(c), one may even conclude that the two modes of the cross as well as that of the corrugations were located around  $710 \text{ nm} \leq \lambda_0 \leq 720$  nm, thus too close to be distinguished.

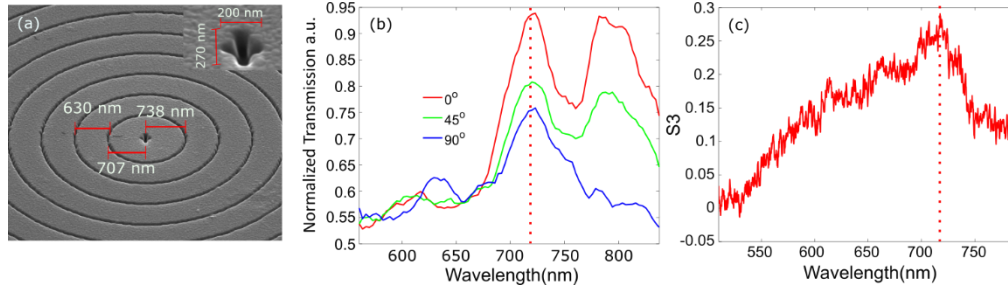


Figure 3: (a) SEM images of the fabricated BE structure with an asymmetric cross-shaped aperture. (b) Normalized transmission through the device. (c)  $S_3$  calculated from the transmitted field.[10]

In summary, despite promising numerical results the experimental data, being subject to fabrication errors, were less than impressive. But the concept was proven which led to an improvement at later stage, see chapter 9 of my thesis [16]. A simpler structure with fewer interlocked effects was the next logical step as described in the following section.

## 3. Biperiodic Array of Circular Holes

Drezet *et al.*[20] proposed a BE structure with periodic elliptical corrugations such that  $a_n = b_n + \delta L$ , where  $\delta L$  is the length difference between the long axis,  $a_n$ , and the short axis,  $b_n$ , of the  $n^{\text{th}}$  concentric ellipse. It was then implied that for the SPP Bloch waves to satisfy the condition to produce CPL, the length difference must simply satisfy  $\delta L \times k_{SPP} = \pi/2$ . However, as I will explain shortly, this approach is inappropriate, given the phase relation is calculated inaccurately and the strength of the two orthogonal surface waves are not considered. Considering a rectangular primitive lattice with constants  $P_x$  and  $P_y$ , for such a plasmonic metasurface to produce a CPL, condition **(A)** dictates  $\Phi_{SPP,x} - \Phi_{SPP,y} = \pi/2$ , where  $\Phi_{SPP,x,y}$  represent the relative phases associated with SPPs propagating along the  $P_x$  and  $P_y$  directions respectively. Condition **(B)** requires the two orthogonal surface modes be equal in amplitudes

to prevent ellipticity. These are the fundamental physical effects used in this report to explain other physical effects which are experimentally confirmed by means of measuring the polarization state of the transmitted light. It is customary among the plasmonic community to quote the following relations governing the surface wave in periodic structures:

$$P = 2\pi \sqrt{i^2 + j^2} / k_{SPP} \quad (7)$$

where

$$k_{SPP} = 2\pi \operatorname{Re} \left[ \sqrt{\varepsilon_m \varepsilon_d / (\varepsilon_m + \varepsilon_d)} \right] / \lambda_0 \quad (8)$$

Using equations (7) and (8), the period of a square array of holes that supports SPPs at its glass/silver interface at  $\lambda_0 = 700$  nm was found to be  $P = \lambda_{SPP} = 433$  nm. Applying Drezet's suggestion to the square array, the detuning in each direction should be given (erroneously) by  $\Delta P = \pm (\pi/4)/k_{SPP} = \pm 54$  nm. However, in *any* periodically patterned surfaces, be it periodic concentric corrugations or hole arrays, one must not ignore the superposition of the forward propagating SPP with its own reflection by the scatterers. In the case of concentric surface corrugations, I have highlighted how the amplitude of a surface waves varies at a scattering point with respect to the scatterer spacings when one takes into account the superposition [14]. In the case of hole arrays, I have discussed the failure of the Bloch theorem in predicting the spectral peaks and proposed a model based on superpositions of surface waves see chapter 6 of my thesis [16]. Given the normal to the surface component of SPPs being an odd function with respect to the center of the hole [14], one may formulate their superposition at the center of the hole,  $(x,y) = (0,0)$  as:

$$\Psi_z(k_{SPP}P_{x,y}) \Big|_{x,y=0} = \frac{1}{3} \left[ \psi_1(0) + \psi_1(2k_{SPP}P_{x,y}) + \psi_2(\pi - k_{SPP}P_{x,y}) \right] \quad (9)$$

where  $\psi_{1,2}(kx) = e^{ikx}$  define waves with a wavenumber,  $k$ , having travelled a distance  $x$ , from its source identified by the subscripts. For schematics see Figure 4(a). To satisfy condition (A), one must calculate the square of the amplitude and the relative phase vs.  $P$  and then obtain the detuning about the center wavelength,  $P = \lambda_{SPP} = 433$  nm from the result, (see Figure 4). The two orthogonal lattice constants are then determined to be  $P \pm \Delta P = 433 \pm 21$  nm, i.e.  $P_x = 412$  nm and  $P_y = 454$  nm.

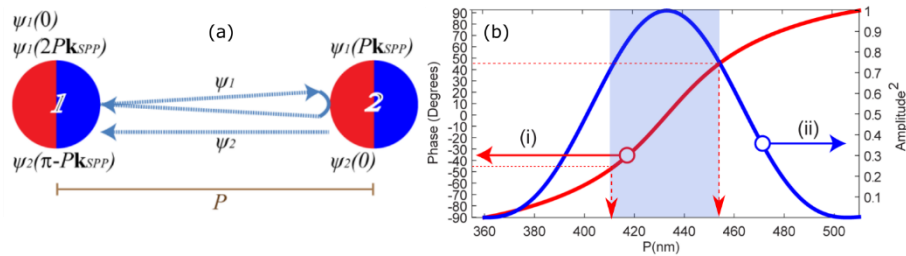


Figure 4: (a) Schematics for two holes interaction via the  $z$ -component of the SPP. (b) The square of the amplitude and the relative phase vs. the  $P$ , analytically calculated for  $k_{SPP} = 2\pi/433$  ( $\text{nm}^{-1}$ ) corresponding to  $\lambda_0 = 700$  nm.

Parallel to the surface components of the SPPs, that are even functions with respect to the center of the hole, hence being responsible for the scattered power [14], may be expressed as:

$$\Psi_{x,y}(k_{SPP}P_{x,y}) \Big|_{x,y=0} = \frac{1}{3} \left[ \psi_1(0) + \psi_1(2k_{SPP}P_{x,y}) + \psi_2(-k_{SPP}P_{x,y}) \right] \quad (10)$$

which also satisfies the condition **(B)**. Stokes parameters and the Degree of Polarization (DOP) for SPPs at the surface and about the lattice point  $(x, y) = (0, 0)$  may be calculated using:

$$S_0|_{x=0} = |\Psi_z(k_{SPP}P_x)|^2 + |\Psi_z(k_{SPP}P_y)|^2 \quad (11)$$

$$S_1|_{x,y=0} = -\left(|\Psi_z(k_{SPP}P_x)|^2 - |\Psi_z(k_{SPP}P_y)|^2\right)/S_0 \quad (12)$$

$$S_2|_{x,y=0} = 2 \operatorname{Re}\left[\Psi_z(k_{SPP}P_x)\Psi_z(k_{SPP}P_y)^*\right]/S_0 \quad (13)$$

$$S_3|_{x,y=0} = -2 \operatorname{Im}\left[\Psi_z(k_{SPP}P_x)\Psi_z(k_{SPP}P_y)^*\right]/S_0 \quad (14)$$

$$\text{DOP} = \sqrt{S_1^2 + S_2^2 + S_3^2} \quad (15)$$

I have also adapted the frequency response function  $R(\omega) = \gamma^2 \omega^2 / \left[ (\omega_0^2 - \omega^2)^2 + \gamma^2 \omega^2 \right]$  [21],

to suit the individual lattice modes  $k_{i,j}$ :

$$R_{i,j} = \gamma_{i,j}^2 k_{SPP}^2 / \left[ (k_{i,j}^2 - k_{SPP}^2)^2 + \gamma_{i,j}^2 k_{SPP}^2 \right] \quad (16)$$

where  $i$  and  $j$  are integers,  $\gamma_{i,j} = k_{i,j} / Q_{i,j}$ ,  $k_{1,0} = 2\pi / P_x$ ,  $k_{0,1} = 2\pi / P_y$ ,

$k_{i,j}|_{i,j \neq 0} = \sqrt{i^2 k_{1,0}^2 + j^2 k_{0,1}^2}$  and  $Q_{i,j}$  is the quality factor for the  $(i, j)$  mode. Figure 5(a) depicts

$R_{i,j}$  with quality factors  $Q_{0,1} = 5$ ,  $Q_{1,1} = 6$  and  $Q_{0,2} = 8$  chosen such that the full-width-half-max of the spectra produced by equation (16) match those produced by equation (10). Peak positions for the (0,1) and (0,2) modes obtained from equation (16), coincide precisely with those obtained from  $\operatorname{Re}\left(\Psi_{x,y}\right)^2|_{x,y=0}$  using equation (10), see Figure 5(b). Stokes parameters and the

DOP calculated from equations (10)-(15) are depicted in Figure 5(c). The superposition also predicts resonances in the vicinity of  $(1,1)_{\text{glass}}$  mode, compare  $R_{1,1}$  in Figure 5(a) to  $\operatorname{Re}\left(\Psi_{x,y}\right)^2|_{x,y=0}$  in Figure 5(b). Given that equation (10) concerns only two holes, that is a 1D

array, resonances in the vicinity of  $(1,1)_{\text{glass}}$  are purely due to the superposition of surface waves and cannot be thought of as lattice modes. So, let's label them as quasi- $(1,1)_{\text{glass}}$  modes for convenience.



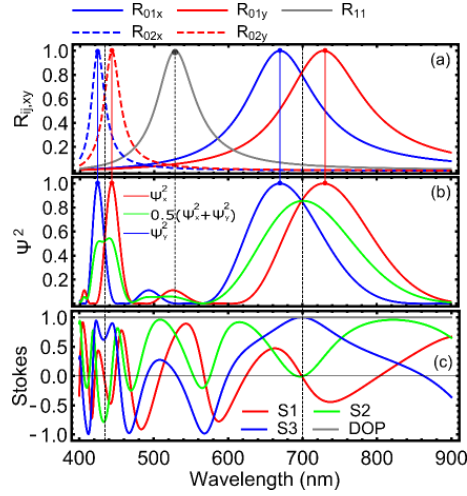


Figure 5: (a)  $R_{i,j}(k_{SPP})$ , (b)  $\text{Re}(\Psi_{x,y})^2|_{x,y=0}$ , (c) Stokes parameters and the DOP calculated from equations (10)-(15).

The model clearly predicts the peak resonances associated with a plasmonic empty lattice and explains the dumping  $\gamma$ . So far, the proposed model was based purely on of surface waves when considering a virtual lattice having no holes. Consequently, many other known and unknown effects relevant to subwavelength apertures are excluded. I have described the numerically modelled array of holes having diameters  $d = 200$  nm perforating a  $h = 100$  nm silver film supported on a glass substrate previously [11, 16], whereby, a 3D model of a unit cell of the array was simulated using Finite Element Method (FEM) using COMSOL Multiphysics/RF module (EM Wave, Frequency Domain) with Stationary Solver. The unit cell consisted of glass/silver/air layers with top/bottom boundaries terminated with scattering boundary condition (SBC). Refractive index of the material filling the hole was set to  $n_h = 1$ . Side boundaries of the unit cell were configured with Periodic Boundary Condition (PBC). Silver film was set in the  $x$ - $y$  plane. Structure was illumination from the glass substrate by an incident wave propagating in the  $+z$  direction for a design wavelength of  $\lambda_0 = 700$  nm under the normal incidence. The electric field was calculated at the top air-side boundary of the cell. The periodicity  $P = 394$  nm corresponded to the fundamental resonant mode  $(1,0)_{\text{glass}}$ . A parametric sweep was performed over  $P_y$ , while keeping  $P_x = 394$  nm. Transmission and relative phase differences between the  $x$  and the  $y$  components of the transmitted electric field were calculated, see Figure 6. The two orthogonal lattice constants,  $P_x \approx 368$  nm and  $P_y \approx 407$  nm satisfied the phase difference of  $90^\circ$ , hence satisfying condition (A). Note that the total detuning  $P_x - P_y = 39$  nm obtained from the simulation is close to the analytical value  $2\Delta P = 42$  nm using equation (9).

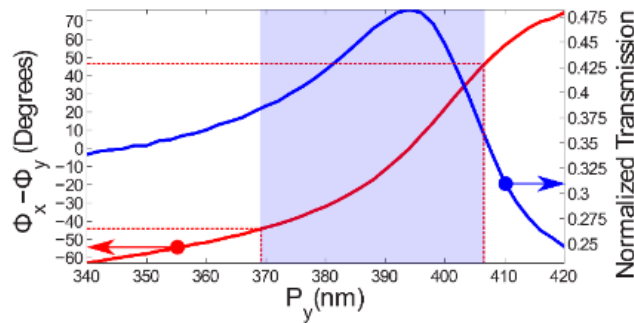


Figure 6: Relative phase differences between the  $x$  and  $y$  components of the transmitted electric field and Absolute transmission (normalized to the intensity over a unit cell) as a function of  $P_y$  for  $P_x = 394$  nm. Reproduced from [11], with the permission of AIP Publishing.

To satisfy condition **(B)**, a parametric sweep over the incident polarization was carried out and the state of polarization of the transmitted light was calculated using:

$$S_0 = |E_{tx}|^2 + |E_{ty}|^2 \quad (17)$$

$$S_1 = |E_{tx}|^2 - |E_{ty}|^2 / S_0 \quad (18)$$

$$S_2 = 2\text{Re}[E_{tx}E_{ty}^*] / S_0 \quad (19)$$

$$S_3 = 2\text{Im}[E_{tx}E_{ty}^*] / S_0 \quad (20)$$

where  $E_{tx}$  and  $E_{ty}$  are the transmitted  $x$  and  $y$  components of the electric field respectively obtained from simulations. The optimum incident polarization at  $\lambda_0 = 700$  nm, was found to be  $\alpha = 47^\circ$ , see Figure 7(a). To explain the optimal values for  $\alpha \neq 45^\circ$ , consider the SPP fields propagating away from a single hole adhering to the complex phasor [22]:

$$E^{SPP} \propto \left( \hat{z} - \frac{i}{K_{SPP}} \rho \right) H_1^{(1)}(k_{SPP} \rho) \cos(\varphi) \quad (21)$$

where the strength of the SPPs is governed by  $\hat{n} \cdot \mathbf{k}_{SPP}$ , due to the dependency on  $\cos(\varphi)$  [23], with  $\hat{n}$  being the normal vector from the cavity to an observation point on the surrounding surface, see figure 29 in [16]. When considering a biperiodic array of holes, there is an optimum incident polarization angle where the SPPs are launched with equal amplitudes in two orthogonal directions, that is:

$$H_1^{(1)}(k_{SPP} P_x) \cos(\alpha) - H_1^{(1)}(k_{SPP} P_y) \sin(\alpha) = 0 \quad (22)$$

The optimum incident polarization angle calculated from equation (22) was found to be  $\alpha = 46.5^\circ$  from the  $x$ -axis of the array and in agreement with that obtained numerically, see Figure 7(a). Same 3D numerical model described above was used to examine the optical response of the device when illuminated from the air and measured from the glass side. Absolute far-field transmission through the device,  $P_t/P_0$ , was calculated for  $\alpha = \{0^\circ, 47^\circ \text{ and } 90^\circ\}$ , where  $P_t$  and  $P_0$  are the transmitted power, through the device and through the glass substrate in the absence of the device respectively, compare Figure 7(b) to Figure 5(b). With  $\alpha = 47^\circ$ , transmitted Stokes parameters were calculated, compare Figure 7(c) to Figure 5(c). Numerically obtained DOP remained precisely unity for all wavelengths as expected. Slight red-shift in the  $(1,1)_{\text{glass}}$  mode, for the change in incident polarization  $\alpha = 0^\circ \rightarrow 90^\circ$ , is somewhat unexpected. No matter the incident polarization, the  $(1,1)_{\text{glass}}$  lattice mode is degenerate and common for all incident polarization. So, I would ascribe the change in momentum to the actual  $(1,1)_{\text{glass}}$  lattice mode (that is invariant) being superposed with the quasi- $(1,1)_{\text{glass}}$  mode that varies with polarization. With the array being illuminated from the air side, one may argue that the strong  $(1,1)_{\text{glass}}$  mode and its red-shift is due to the superposition of  $(1,1)_{\text{glass}}$  and  $(1,0)_{\text{air}}$  modes. However, I have demonstrated the optical response of an array of holes with  $n_h = 1$ , supported on a glass substrate, is dominated by glass modes regardless, please see section 6.3 of my thesis[16].

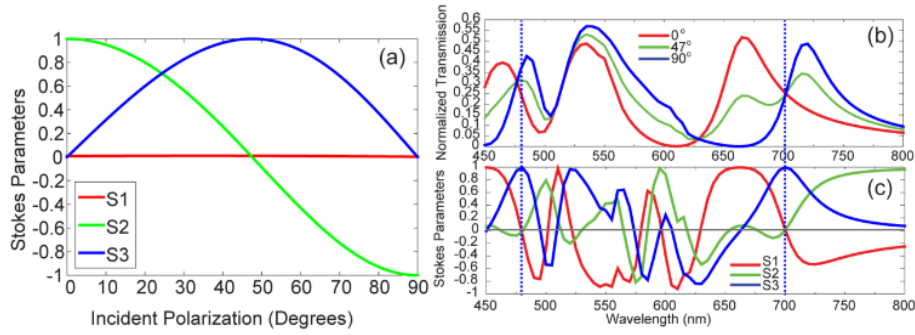


Figure 7: Spectra of the hole array having periodicities  $P_x = 368$  and  $P_y = 407$  nm. (a) Stokes parameters vs. the incident polarization. (b) Absolute transmission vs. the wavelength, when incident field is at polarizations  $0^\circ$ ,  $90^\circ$  and  $47^\circ$ . (c) Stokes parameters vs. the wavelength when incident polarization is  $47^\circ$ .

### 3.1 Significant Observations and Applications

#### 3.1.1 Extraordinary Optical Transmission: (The Mechanism)

The two somewhat peculiar observations are: (1.a): *The formation of surface charges at the glass/silver interface when the device was illuminated from the air side where no SPP mode is supported at air/silver interface for the resonant wavelength  $\lambda_0 = 700$  nm.* This was also highlighted in my theses, see section 6.3 [16]. (1.b): *The state of polarization of the transmitted light with  $S_3 = 1$  and yet  $S_1 = S_2 = 0$  when the incident light is linearly polarized at  $\alpha = 47^\circ$ .*

From (1.a) and (1.b) one can develop a clear picture on the origin of Extraordinary Optical Transmission (EOT) [24] that is to say: *no light was transmitted through the hole directly.* Consequently, the transmission of power through the device must have pertained to the following steps: (i) excitations of LSPs inside the holes by the incident light, (ii) launching of the SPPs by the LSPs, hence LSP-SPP coupling and (iii) partial scattering of the LSP/SPPs in the form of free propagating EM waves. This is true at least in the case of a plasmonic hole array modelled here, when the dimensions of the hole were not optimized for the target wavelength. In other cases/devices, there may also be a direct transmission through the hole that superpose what I just described.

#### 3.1.2 Rotating Surface Charge Densities and Dipole Moments

What happens to the surface charges when both conditions **(A)** and **(B)** are satisfied? Figure 8(a) shows the entire unit cell and the transmitted electric field showing CPL state of polarization when the device was normally illuminated from the glass side with  $\alpha = 47^\circ$  and  $\lambda_0 = 700$  nm. Figure 8(b)-(c) depicts the respective surface charge densities at silver/air and silver/glass interfaces. An extended model consisting of nine unit-cells in a 3-by-3 array formation was also simulated. Figure 8(d) represents the top view of the simulated surface charge densities at the silver/glass interface of the 3x3 model, when the device was normally illuminated from the air side with  $\alpha = 47^\circ$  at design wavelength  $\lambda_0 = 700$  nm and at  $t = \{0, T/8, T/4, 3T/8\}$ , where  $T$ , is the period of the optical wave.

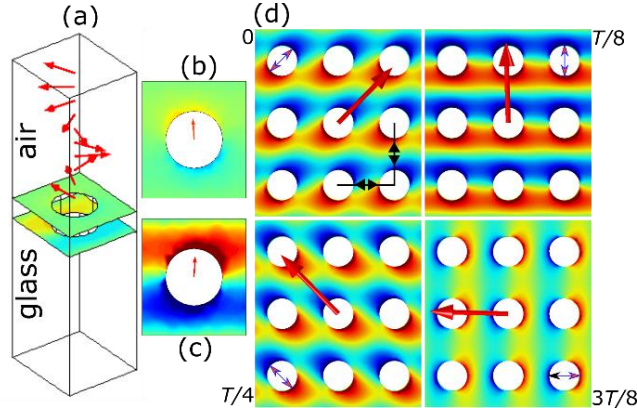


Figure 8: Surface charge density (red = 1, blue = -1 and green = 0) and the transmitted electric field vector represented by red arrows, calculated (a) within the entire of the unit cell (b) at air/silver interface of the unit cell, (c) at glass/silver interface the unit cell (d) at glass/silver interface of a 3x3 array, at  $t = \{0, T/8, T/4, 3T/8\}$ , where  $T$  is the period. Double arrow-heads show the orientation of the virtual dipole moments associated with the charge impurity formed on the rims of the holes. Reproduced from [11], with the permission of AIP Publishing.

The consequence of rotating surface charge density on the rims of the holes are (2.a): *the formation of rotating dipole moments,  $\mu_e$ , governed by equation (2) at the lattice points* and (2.b) *dipolar formations between a hole and its eight nearest neighbors that are discrete in time, occurring every  $T/8$* . The latter being more peculiar than the former given that it occurs at  $\lambda_0 = 700$  nm where the only supported mode is supposed to be  $(1,0)_{\text{glass}}$ , a clear breakdown of equations (7) and (8).

### 3.1.3 Three Level Quantum System

One may consider a biperiodic plasmonic hole array as a quantum interferometer with interesting properties. The most significant observation in that regard is (3.a): *the DOP = 1 for the transmitted light at all wavelengths*. If one considers the Stokes parameters as a probability amplitude of a quantum system, the fact that DOP remains unity for all wavelengths becomes significant. Owing to their strong correlation via equations (17)-(20) (or equations (9) & (11)-(14) in the case of analytical solutions), a quantum system that satisfy probability sum  $S_1^2 + S_2^2 + S_3^2 = 1$ , doesn't suffer from *depolarization* (that is a form of quantum decoherence). Therefore, above model with its two orthogonal modes is well suited to describe a *three-level quantum system for two (or more) entangled photons*. Consequently, for a given incident polarization and wavelength,  $(\alpha, \lambda_0)$ , one may define the three-level mixed state of polarizations for multi photons, as:

$$\left| \psi_{(\alpha, \lambda)} \right\rangle_{x, y=0} = S_{1(\alpha, \lambda)} |+\rangle + S_{2(\alpha, \lambda)} |x\rangle + S_{3(\alpha, \lambda)} |O\rangle \quad (23)$$

where  $|+\rangle, |x\rangle$  &  $|O\rangle$  represent the *single* level pure states of polarization with  $S_1, S_2, S_3$  being the probability amplitudes that range from -1 to 1. Each pure state encapsulates the  $x$  and  $y$ -polarized photons with  $|+\rangle \equiv |x\rangle$ ,  $-|+\rangle \equiv |y\rangle$ ,  $\pm|x\rangle \equiv \frac{1}{\sqrt{2}}(|x\rangle \pm |y\rangle)$  and  $\pm|O\rangle \equiv \frac{1}{\sqrt{2}}(|x\rangle \pm i|y\rangle)$

, compare the last two definitions to equations (3)-(4). The negative probability amplitudes do not violate the superposition principle in (23). With that in mind, Figure 7(c) maps all possible states in Hilbert space, for this particular hole array, that is for the given choice of incident polarization, material and dimension as stated in the previous section. Now, what formalism/algorithm must be implemented based on equation (23) and how this could play a

role in quantum computation/information/cryptography deserves further study but is beyond the scope of this report. Notably, every mixed state  $|\psi_{(\alpha,\lambda)}\rangle$  indexed by a particular incident polarization and wavelength,  $(\alpha_i, \lambda_j)$ , has its own probability amplitude, governed by the normalized transmission  $I = P_i/P_0$ . Consequently, when the device is excited with an incandescent incident unpolarized light, the state of the system as a whole must be denoted by:

$$\psi_{system} = \sum_{i,j} c_{(\alpha_i,\lambda_j)} |\psi_{(\alpha_i,\lambda_j)}\rangle \quad (24)$$

Where the normalized portability amplitudes are given by:

$$c(\alpha_i,\lambda_j) = I(\alpha_i,\lambda_j) / \int_{\alpha_i}^{\alpha_f} \int_{\lambda_i}^{\lambda_f} I(\alpha,\lambda) d\lambda d\alpha \quad (25)$$

Equation (24) implies that the state of the system as a whole is further, the result of superposition of individual states  $|\psi_{(\alpha_i,\lambda_j)}\rangle$ . But do they form an orthonormal basis on their own? I will address this question in the experimental section. However, for the particular incident polarization  $\alpha = 47^\circ$  and the wavelength range that produced the spectrum in Figure 7(b)-(line in green), equation (25) maybe reduced to  $c(47^\circ, 700nm) = I(47^\circ, 700nm) / \int_{450nm}^{800nm} I(\lambda) d\lambda$ . On the other hand, one may even add another parameter to equation (25) by considering the angle of incidence. So, there is room to play.

### 3.1.4 Applications in Gravitational Decoherence

Recently I came across two articles on ‘‘Gravitational Decoherence’’.

Anastopoulos and Hu [25] defining the intrinsic or fundamental decoherence as, and I quote: *’’Intrinsic or fundamental decoherence refers to some intrinsic or fundamental conditions or processes which engender decoherence in varying degrees but universal to all quantum systems. This could come from (or could account for) the uncertainty relation, some fundamental imprecision in the measuring devices (starting with clocks and rulers), in the dynamics, or in treating time as a statistical variable’’* [25].

Bachlechner [26] wrote: *‘‘The decoherence effect can be modeled as a quantum Zeno effect in which the wave function of the tunneling field ‘‘collapses’’ to a classical configuration each time the background leaks information to the environment about whether a bubble exists or not.’’*[26].

DOP = 1 in the model I report here, infers a quantum system that is deterministic with no *uncertainty relation*. This is true at least in theory given that the numerical model of the array represents an ideal system that interacts only with light when there is no *imprecision in the measuring devices* or any other external factor causing decoherence. I am not an expert in gravitation but if I understood the two reports correctly, I would propose that the device I reported here, may have an application in detecting gravitational decoherence by monitoring and anticipating the collapse of the wave function that would result in DOP fluctuations.

Furthermore, considering two identical biperiodic hole arrays {array1, array2}, acting as a transmitter and a receiver, when the first device is excited by a linearly polarized light, and the resulting transmitted CPL be an input to the second device, the transmitted light through the second device would be a linearly polarized light with the original incident angle of polarization. In other words:

$$(A|+\rangle + B|\times\rangle) \xrightarrow{input1} [array1] \xrightarrow{output1} |O\rangle \xrightarrow{input2} [array2] \xrightarrow{output2} (A'|+\rangle + B'|\times\rangle) \quad (26)$$

Where  $A' = A$  &  $B' = B$ , and this was confirmed numerically. Deployment of two identical arrays positioned far apart, coupled via the state of CPL,  $|\circ\rangle$ , must be looked upon as two arrays of quantum interferometers that are coupled. In this case, any gravitational decoherence that may impact the optical responses of either or both devices, would result in a final state other than the initial state, where  $A' \neq A$  and/or  $B' \neq B$ . The motivation of implementing two coupled quantum optical device is to increase the sensitivity of the system as a whole with respect to gravitation decoherence.

### 3.1.5 Applications in Detecting Gravitational Waves

Fundamental physics governing Michelson interferometers is that of the interference whereby the passage of the two monochromatic beams of the same wavelength through equal/unequal optical paths and their superposition afterwards would create either constructive or destructive interference at the point of detection. Circularly polarized light in conjunction with biperiodic arrays may play an important role in detecting gravitational waves as well as revealing more about their nature. The question is by how much these two conditions **(A)** and **(B)**, as stated in the introduction, are violated by gravitational waves. Furthermore, considering the second part

of equation (26), i.e.  $|\circ\rangle \xrightarrow{\text{input 2}} [\text{array 2}] \xrightarrow{\text{output 2}} (A'|+\rangle + B'|\times\rangle)$ , it is apparent that the role of the array is that of a polarization converter, that is to convert an incoming CPL into an outgoing linearly polarized light (LPL). It is, therefore, possible to design an interferometer based on polarized light that would isolate the two orthogonal polarization states, hence study the impact of gravitational waves on each type of polarization.

I would propose an alteration to Michelson interferometer based on polarized light as depicted in Figure 9. The black box labelled as Source/Splitter/Polarizer/Combiner, generates a coherent and monochromatic light which is then split into horizontally/vertically polarized lights (denoted by  $\alpha = 0^\circ$  and  $\alpha = 90^\circ$  in the figure), with each type polarization being routed to the relevant arm of the interferometer. Armlengths with  $L_1 \neq L_2$  are set in such ways to bring about the  $90^\circ$  phase difference between the two beams, upon their reflection back to the black box, i.e. after having travelled  $2L_1$  and  $2L_2$ . The two beams are then superposed to produce a single beam that is circularly polarized. CPL is then forwarded to a detector consisting of a plasmonic biperiodic array (i.e. an array of quantum interferometers) that converts CPL to LPL with a well-defined polarization axis. An analyzer with its polarization axis adjusted to the incoming LPL, serves as filter allowing/blocking the passage of photons to the counter. Any changes to the beam along the  $L_1$  or  $L_2$  would result in distortion of the resultant CPL in the form induced ellipticity which in turn would result in the change in the polarization axis of photon that fall on the analyzer, hence change in photon count. The amplitude of the interference also plays the same role as Michelson interferometers which also impact the number of photon detected. In the figure I have considered two distinct scenarios, when the gravitational is either normal to  $L_1$ , or to  $L_2$ . Apart from a new interferometer design, the aim is to study the impact of gravitational waves on polarized of light.

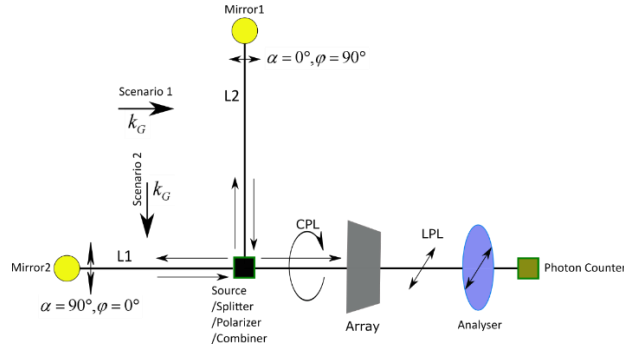


Figure 9: Schematics of an interferometer based on polarized light with a plasmonic biperiodic array and an analyser and a photon counter as an integrated detector.

### 3.2 Experimental Demonstration

The device was first fabricated with a silver film on a glass substrate and was reported in [11, 16], see Figure 10.

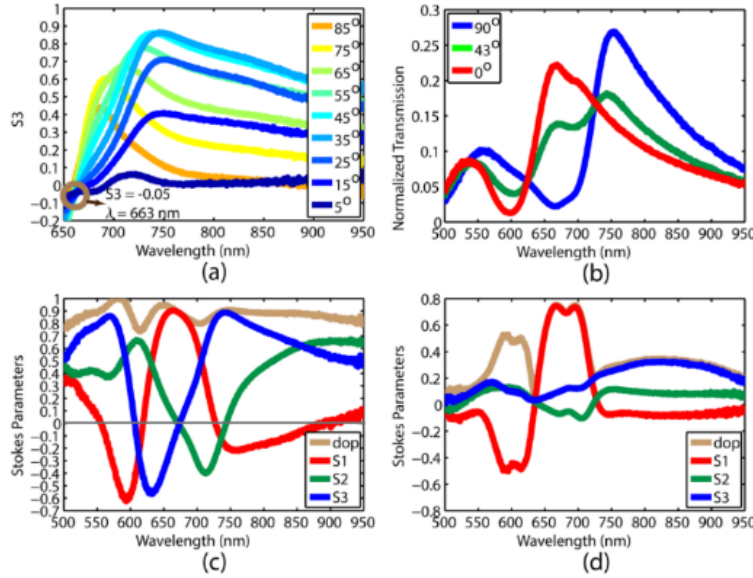


Figure 10: Experimental data: (a) Transmitted  $S_3$  spectra for incident polarizations  $5^\circ \leq \alpha \leq 85^\circ$ . (b) Absolute transmission when incident field is at polarizations  $90^\circ$ ,  $43^\circ$  and  $0^\circ$ . (c) Stokes parameters vs. the wavelength for incident polarization  $43^\circ$ . (d) Stokes parameters vs. the wavelength for un-polarized normally incident light. Reproduced from [11], with the permission of AIP Publishing.

Earlier simulations showed improvement in transmission through a hole array when it is set in a homogeneous environment with the substrate, superstrate and the hole having the same refractive indices, see section 6.2 of my thesis[16] (i.e.  $n_1 = n_2 = n_3$ ). As for transmitted CPL, previous experiment had resulted in  $S_3 < 1$ , that contradicted my numerical results. So, I implemented the technique suggested by Kihara [27] that catered for phase errors associated with the optical elements, that confirmed  $S_3 = 1$  is indeed possible, see Figure 11. With the new device, criteria **(I)**- **(II)** were satisfied in full. I have elaborated on the fabrication method, measurement techniques and numerical/experimental results in details in [12, 16].

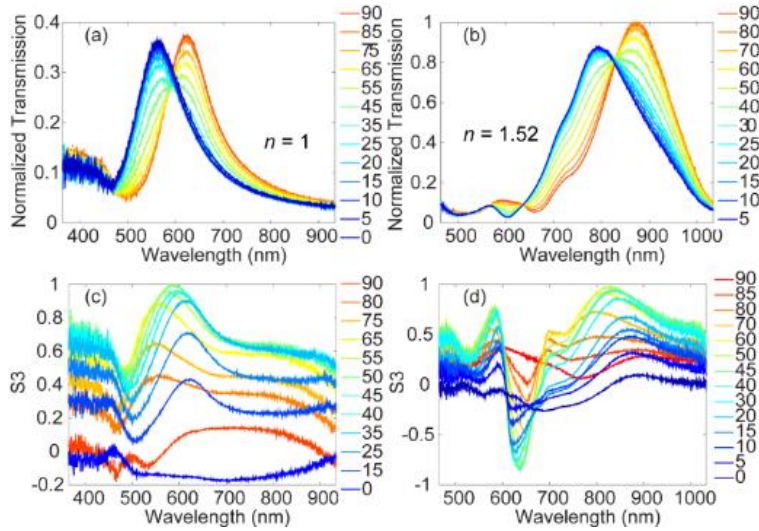


Figure 11: Experimentally obtained results for incident polarization  $0^\circ \leq \alpha \leq 90^\circ$ . Absolute transmission vs. the wavelength for (a)  $n_1 = n_2 = n_3 = 1$  and (b)  $n_1 = n_2 = n_3 = 1.52$ .  $S_3$  vs. the wavelength for (c)  $n_1 = n_2 = n_3 = 1$  and (d)  $n_1 = n_2 = n_3 = 1.52$ . Reproduced from [12], with the permission of OSA Publishing .

### 3.2.1 An Argument on Number of Photons and Their Spins

The most important aspect of the experimental setup in this report was the use of Andor Shamrock 303i-A spectrometer (with Andor iDus DU920P-BR-DD CCD) which I believe is a highly accurate instrument in counting the number of photons per frequency/wavelength. And notably, although the spectra presented are normalized, they are indicative of photon counts. This is important as I will shortly address the dilemma I was facing with respect to quantum presentation of the spin of a photon.

Although, in my opinion, it is acceptable to use  $\pm\hbar$  as a *notion* to refer to  $\pm|\circ\rangle$  polarization state of *light*, as I have done in section 2.3 of my master thesis [9], I do not support the idea of a *single* photon having a  $+\hbar$  or  $-\hbar$  spin, for example as asserted in section “8.1.4 Angular Momentum and Photon Picture” in [28]. In classical optics, it is a well-known fact that the a linearly polarized light may be constructed from the superposition of two opposite circular polarized light. In providing an explanation for linearly polarized photon, however, Hecht exerts a similar principle whereby each photon in a linearly polarized light must exist in either  $+\hbar$  or  $-\hbar$  state with equal probabilities, as nothing is known about the state of a photon before measurements. To my opinion, while the classical picture of linearly polarized light is valid, the latter is a flawed, as it implies that somehow optical elements dictates the spin of a photon upon measurements. Note that a 50/50 percent chance of a photon being in  $+\hbar$  or  $-\hbar$  state, best fits a description of an unpolarized light prior to polarization but not a linearly polarized photon before being analyzed.

Such disparities between quantum and classical picture of photon and light has created confusion ever since the introduction photon. I intend no criticism of any author, as I believe Hecht and others were merely inferring and reporting on the scientific consensus of the time. Referencing a very popular book in optics has historical reasons and I am certain many who study classical electromagnetism have struggled grasping the concept of single photon with a spin, just as I did. And I hope a clear picture of the polarization of photons would emerge as the result of this report.



With respect to my experimental findings in this report, one may assert that the optical response of the device to the excitation incident light polarized at  $\alpha = 0^\circ$  and  $\alpha = 90^\circ$ , as seen in Figure 10 and Figure 11, corresponds to all horizontally and vertically polarized photons with no spin. For example, the line in blue as seen in Figure 11(b) represents the wavelength positions of all the horizontally polarized photons detected by the instrument, when the incident light was polarized at  $\alpha = 0^\circ$ , whereas the line in red corresponds to all the vertically polarized photons when the device was excited with light polarized at  $\alpha = 90^\circ$ . Consequently, we must accept that a single photon has no spin, otherwise every experiment based on vertically/horizontally polarized photons, such as those reported in chapter 14 of Quantum Optics by Fox [4], must be considered invalid.

Going back to Figure 11(b), notably the two curves intercept at  $\lambda_0 = 820$  nm. Clearly this is the wavelength at which the device is capable of producing equal number of both kinds of photons. This condition is satisfied for some incident polarization,  $45^\circ \leq \alpha \leq 50^\circ$ , and given the phase difference between the two kinds of photons,  $S_3 = 1$  is achieved at  $\lambda_0 = 820$  nm. I can then infer that the photon requirement to produce a light with  $\pm\hbar$ , hence its resultant electric field rotating about  $\mathbf{k}_0$ , are just the same as those described in the introduction, i.e. the adherence to conditions (A) and (B). Meaning, we need at least two photons with same energy (one vertically and the other horizontally polarized) with a phase difference of  $90^\circ$  between their propagation. Hypothetically, it is possible to adjust the intensity of the incident beam for two such photons be emitted by device at a time, eliminating the need for any integrated single photon emitters. My definition of such two photons as being in an *entangled state*, refers to a single quantum system, be it vacuum, consisting of two photons with their coherent time and length extended to the far-field if not infinity, yet representing polarization state that is only possible while the constituting photons remain part of the quantum system, interacting with one another via their individual orthogonal polarizations.

I have retained my raw data files showing the photon counts ...etc. and have revisited them multiple times in search for new findings and I will continue to do so. Upon any new discovery in contrary to what I have stated here, I will make the required adjustments.

### 3.2.1 Encapsulation of Three Level Quantum State into a Continuous orthonormal set

Notably, analytical and numerical results were carried out with a single wavelength at the time, whereas the experimental results were obtained by exciting the array using a white light. Therefore, it was important to determine whether multiwavelength excitation of the array had any impact on the spectra. In the experiment I report here, the array was illuminated from both sides using two independent light sources. From the glass/silver side the array was illuminated with a Fianium Supercontinuum light source filtered at  $525 < \lambda_0 < 560$  nm. The filter also allowed partial transmission at  $435 < \lambda_0 < 450$  nm. These coincided with the  $(1,1)_{\text{glass}}$  and  $(0,2)_{\text{glass}}$  modes along the  $x$ -direction. Number of photons detected from the Fianium Supercontinuum light source passing through the filter vs the wavelength in the absence of the device is depicted in Figure 12(a) and inset. Spectra in red and green are produced with  $q = 400$  and  $q = 420$  respectively. Here,  $q$ , is the quality factor that determines the output power and the spectral line profile of the Fianium's emission, with  $q = 0$  meaning no emission. With the device in place, in order to excite all modes associated with  $P_x$ , the array was first illuminated normally from the air/silver side with a halogen light polarized at  $\alpha = 0^\circ$ . The Fianium power was then changed from  $q = 0$  to  $q = 400$  to  $q = 420$ . Figure 12(b) shows the transmission spectra of the polarized halogen light through the device superposed by reflection spectra of the filtered Fianium light source from the device as detected by the spectrometer. Figure 12(c)-(d) are the selected regions from Figure 12(b). This exercise is not about percent reflection/transmission from/through the device. The main motivation behind this work was to detect any noticeable change in amplitude or phase, in the  $(1,0)_{\text{glass}}$  when  $(1,1)_{\text{glass}}$  or  $(2,0)_{\text{glass}}$  modes are perturbed. Jitters observed in the  $(1,0)_{\text{glass}}$ , Figure 12(d), are present for all  $q$  values, hence attributed to the

thermal instability of SPPs and perhaps the optical instruments and light sources. Considering the photon counts by which the  $(1,1)_{\text{glass}}$  is perturbed vs the perturbation observed in  $(1,0)_{\text{glass}}$ , it is safe to conclude that although multiple SPP-Bloch modes can coexist, coupling between them (if any) is insignificant. This has an important ramification, that is  $\langle \psi_{(\alpha,\lambda_j)} | \psi_{(\alpha,\lambda_i)} \rangle = \delta_{ij}$ . Depending on how one considers the wavelength divisions, states  $c_{(\alpha,\lambda_i)} | \psi_{(\alpha,\lambda_i)} \rangle$ , can now form a *continuous orthonormal set*, with each  $| \psi_{(\alpha,\lambda_i)} \rangle$  perceived as a pure quantum state on its own.

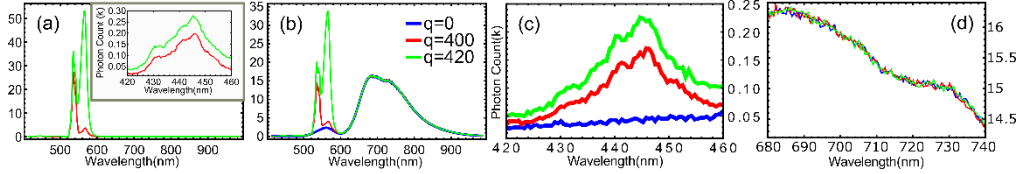


Figure 12: (a) Photon count detected from the Fianium Supercontinuum light source passing through the filter vs the wavelength in the absence of the device. (b) Transmission spectra of the polarized halogen light through the device superposed with the reflection spectra of the filtered Fianium light source from the device as detected by the spectrometer. Spectra in blue, red green are produced with  $q = 0$ ,  $q = 400$  and  $q = 420$  respectively. (c) and (d) selected regions from (b).

#### 4. Conclusion

I have discussed the concept resultant dipole moment starting from a simple asymmetric cross-shaped nano-antenna to a simple biperiodic array of holes. A clear link between resultant dipole moment, LSPs, SPPs, and the transmitted Stokes parameters was established, hence the Dipole-LSP-SPP-Stokes coupling. I have shown how a simple analytical model based on superposition of waves between two holes can predict plasmonic lattice modes. In addition, the analytical model identifies quasi-modes which explains the anomalous shift in  $(1,1)$  modes. Stokes parameters obtained analytically are in accordance with those obtained numerically. The cyclic plasmonic wavevector that and the subsequent cyclic plasmonic dipole moments are further the direct consequent of the superposition of two orthogonal surface waves when  $S_3 = 1$ . When examining the surface waves, a biperiodic array with two unequal pathlengths, functions as an array of coherent quantum interferometers. I have explained how the state of polarization of such array may be considered as states in a three-basis quantum system. Furthermore, I have shown that SPP-Bloch modes do not interact with one another. That may provide an opportunity for the realization of a quantum system with a continuous orthonormal set, i.e. a quantum system with many-basis. I have also highlighted aspects of the device applicable to generation/detection of entangled photons, and how any two such array may be coupled to achieve that. I also hypothesized on a possible application in gravitational decoherence, however, what was suggested was mere possibility hoping to ignite interest in bridging plasmonics to other field of physics.

#### Disclosures

The authors declare that there are no conflicts of interest related to this article.

#### References

1. S. Strauf, N. G. Stoltz, M. T. Rakher, L. A. Coldren, P. M. Petroff, and D. Bouwmeester, "High-frequency single-photon source with polarization control," *Nat. Photonics* **1**, 704-708 (2007).
2. N. Gisin, G. G. Ribordy, W. Tittel, and H. Zbinden, "Quantum cryptography," *Rev. Mod. Phys.* **74**, 145-195 (2002).
3. L. M. Duan, J. I. Cirac, P. Zoller, and E. S. Polzik, "Quantum communication between atomic ensembles using coherent light," *Phys. Rev. Lett.* **85**, 5643-5646 (2000).
4. M. Fox, *Quantum optics : an introduction*, Oxford master series in physics (Oxford University Press, Oxford ; New York, 2006), pp. xvii, 378 p.

5. Y. Shih, *An introduction to quantum optics : photon and biphoton physics*, Series in optics and optoelectronics (CRC Press, Boca Raton, FL, 2011), pp. xix, 464 p.
6. M. D. Eisaman, J. Fan, A. Migdall, and S. V. Polyakov, "Invited Review Article: Single-photon sources and detectors," *Rev. Sci. Instrum.* **82**(2011).
7. A. K. Ekert, "Quantum Cryptography Based On Bell Theorem," *Phys. Rev. Lett.* **67**, 661-663 (1991).
8. M. A. Nielsen and I. L. Chuang, *Quantum computation and quantum information* (Cambridge University Press, Cambridge ; New York, 2000), pp. xxv, 676 p.
9. A. Djalalian Assl, "Tailoring Properties of Magneto-Optical Crystals," Student thesis 2010).
10. A. Djalalian-Assl, J. Cadusch, T. D. James, T. J. Davis, and A. Roberts, "Polarization effect and emission control in asymmetric cross-shaped slot antennas surrounded with periodic corrugations," in *Micro/Nano Materials, Devices, and Systems*, Proceedings of SPIE (Spie-Int Soc Optical Engineering, 2013),
11. A. Djalalian-Assl, J. J. Cadusch, Z. Q. Teo, T. J. Davis, and A. Roberts, "Surface plasmon wave plates," *Appl. Phys. Lett.* **106**, 041104 (2015).
12. A. Djalalian-Assl, J. J. Cadusch, E. Balaur, and M. Aramesh, "Tunable surface plasmon wave plates," *Opt. Lett.* **41**, 3146-3148 (2016).
13. P. Lorrain, D. R. Corson, and F. o. Lorrain, *Electromagnetic fields and waves : including electric circuits*, 3rd ed. (Freeman, New York, 1988), pp. xiii, 754 p.
14. A. Djalalian-Assl, "Dipole Emission to Surface Plasmon-Coupled Enhanced Transmission in Diamond Substrates with Nitrogen Vacancy Center- Near the Surface," *Photonics* **4**, 10 (2017).
15. A. Djalalian-Assl, X. M. Goh, A. Roberts, and T. J. Davis, "Optical Nano-antennas," in *Proceedings of the International Quantum Electronics Conference and Conference on Lasers and Electro-Optics Pacific Rim 2011*, (Optical Society of America, 2011), J824.
16. A. Djalalian-Assl, "Optical nano-antennas," PhD (The University of Melbourne, Melbourne, 2015).
17. A. Djalalian-Assl, D. E. Gomez, A. Roberts, and T. J. Davis, "Frequency-dependent optical steering from subwavelength plasmonic structures," *Opt. Lett.* **37**, 4206-4208 (2012).
18. M. A. Omar, *Elementary solid state physics : principles and applications*, Solid State Science (Addison-Wesley Pub. Co., 1975).
19. A. Djalalian-Assl, "Propagating surface plasmons with an interference envelope and a vision for time crystals," *OSA Continuum* **1**, 462-476 (2018).
20. A. Drezet, C. Genet, and T. W. Ebbesen, "Miniature plasmonic wave plates," *Phys. Rev. Lett.* **101**(2008).
21. I. G. Main, *Vibrations and Waves in Physics* (Cambridge University Press, 1987).
22. S. H. Chang, S. K. Gray, and G. C. Schatz, "Surface plasmon generation and light transmission by isolated nanoholes and arrays of nanoholes in thin metal films," *Opt. Express* **13**, 3150-3165 (2005).
23. L. L. Yin, V. K. Vlasko-Vlasov, J. Pearson, J. M. Hiller, J. Hua, U. Welp, D. E. Brown, and C. W. Kimball, "Subwavelength focusing and guiding of surface plasmons," *Nano Lett.* **5**, 1399-1402 (2005).
24. T. W. Ebbesen, H. J. Lezec, H. F. Ghaemi, T. Thio, and P. A. Wolff, "Extraordinary optical transmission through sub-wavelength hole arrays," *Nat.* **391**, 667-669 (1998).
25. C. Anastopoulos and B. L. Hu, "A master equation for gravitational decoherence: probing the textures of spacetime," *Classical and Quantum Gravity* **30**, 165007 (2013).
26. C. B. Thomas, "Decoherence delays false vacuum decay," *Classical and Quantum Gravity* **30**, 095012 (2013).
27. T. Kihara, "Measurement method of Stokes parameters using a quarter-wave plate with phase difference errors," *Appl. Opt.* **50**, 2582-2587 (2011).
28. E. Hecht, *Optics*, 2nd ed. (Reading, Mass, Addison-Wesley Pub. Co, 1987).